Direct Reconstruction of Kinetic Parameter Images From Dynamic PET Data

M. E. Kamasak*, C. A. Bouman, E. D. Morris, and K. Sauer

***Abstract*—Our goal in this paper is the estimation of kinetic model parameters for each voxel corresponding to a dense three-dimensional (3-D) positron emission tomography (PET) image. Typically, the activity images are first reconstructed from PET sinogram frames at each measurement time, and then the kinetic parameters are estimated by fitting a model to the reconstructed time-activity response of each voxel. However, this "indirect" approach to kinetic parameter estimation tends to reduce signal-to-noise ratio (SNR) because of the requirement that the sinogram data be divided into individual time frames.**

In 1985, Carson and Lange proposed [1], but did not implement, a method based on the expectation-maximization (EM) algorithm for direct parametric reconstruction. The approach is "direct" because it estimates the optimal kinetic parameters directly from the sinogram data, without an intermediate reconstruction step. However, direct voxel-wise parametric reconstruction remained a challenge due to the unsolved complexities of inversion and spatial regularization.

In this paper, we demonstrate and evaluate a new and efficient method for direct voxel-wise reconstruction of kinetic parameter images using all frames of the PET data. The direct parametric image reconstruction is formulated in a Bayesian framework, and uses the parametric iterative coordinate descent (PICD) algorithm to solve the resulting optimization problem [2]. The PICD algorithm is computationally efficient and is implemented with spatial regularization in the domain of the physiologically relevant parameters. Our experimental simulations of a rat head imaged in a working small animal scanner indicate that direct parametric reconstruction can substantially reduce root-mean-squared error (RMSE) in the estimation of kinetic parameters, as compared to indirect methods, without appreciably increasing computation.

***Index Terms*—Dynamic PET, iterative reconstruction, kinetic modeling, regularization, tomography.**

I. Introduction

POSITRON emission tomography (PET) is a powerful molecular imaging technique with the sensitivity to detect picomolar quantities of a labeled tracer with reasonable (seconds to minutes) temporal resolution. Through the application of kinetic models, the dynamic PET data can be transformed into physiological parameters that indicate the functional state of the imaged tissue. Ideally, one would like to reconstruct parametric images from PET data i.e., images which specify the estimated kinetic parameters for each voxel in the imaged volume. Such parametric images could serve many uses. For example, they may be particularly desirable when testing a new tracer whose sites of action are not completely known. In the brain, parametric images might be useful in identifying new brain circuits or discovering unsuspected connectivity between disparate brain regions. As new tracers continue to be developed with greater specific to nonspecific binding ratios, the impetus grows for looking at their uptake in all regions of the brain, rather than in a few preselected regions of interest. For example, $[^{18}F]$-fallypride, a high affinity dopamine tracer, can be used to image dopamine receptors outside the striatum because the nonspecific background is low [3].

This paper introduces a novel algorithm for directly reconstructing parametric images from PET sinogram data. We demonstrate that this method can generate parametric images with superior quality; and, perhaps surprisingly, we also show that it has computational requirements that are similar to a two-step approach of iterative reconstruction followed by kinetic parameter estimation.

Kinetic compartmental models are often used to describe the movement of a tracer between different physically or chemically distinct states or compartments [4]–[6]. The exchange of tracer between these compartments can be modeled by a system of first-order ordinary differential equations (ODEs) whose coefficients are the kinetic parameters. The resulting kinetic models have been validated as producing reliable quantitative indexes of various clinically and scientifically important physiological processes [7]–[17].

In some cases, a single set of kinetic parameters can describe the tracer behavior in a homogeneous region of tissue such as the myocardium or perhaps the entire striatum in brain images. If the region of interest can be delineated using some form of segmentation, then the PET activity can be averaged over the region at each time frame and a single set of kinetic parameters can be estimated by fitting a single kinetic model to the time sequence of average activities. This case is illustrated in Fig. 1. The PET data are first reconstructed into K time frames, then a region of interest (ROI) is segmented from each frame, and a single set of kinetic parameters is fit to the regional-average time sequence. These ROI-based methods may be further classified into linear methods and nonlinear methods. Linear techniques [18]–[23] transform the data, so that the parameters of interest can be estimated by linear regression methods, while nonlinear techniques

Manuscript received September 24, 2004; revised February 1, 2005. The Associate Editor responsible for coordinating the review of this paper and recommending its publication was D. Townsend. *Asterisk indicates corresponding author.*

*M. E. Kamasak is with the School of Electrical and Computer Engineering, Purdue University, 1285 EE Building, P. O. 268, West Lafayette, IN 47907 USA (e-mail: kamasak@purdue.edu).

C. A. Bouman is with the School of Electrical and Computer Engineering, Purdue University, West Lafayette, IN 47907 (e-mail: bouman@ecn.purdue.edu).

E. D. Morris is with the Indiana University, Purdue University-Indianapolis Radiology and Biomedical Engineering Departments, Indianapolis, IN 46202 USA. (e-mail: emorris@iupui.edu)

K. Sauer is with the Department of Electrical Engineering, University of Notre Dame, Notre Dame, IN 46556 USA (e-mail: sauer@nd.edu).

Digital Object Identifier 10.1109/TMI.2005.845317

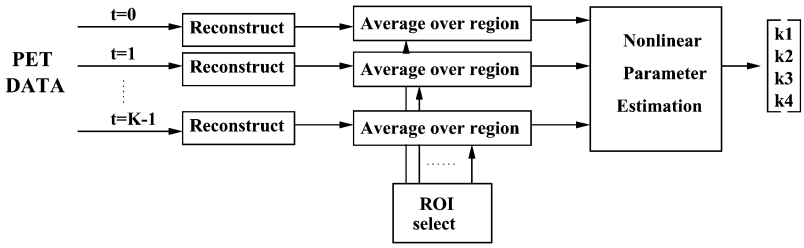

Fig. 1. ROI-based kinetic parameter estimation methods.

[5], [6] generally estimate the kinetic parameters by iteratively minimizing a properly weighted distance metric between the reconstructed time-activity curves and the model output.

Recently, there has been increasing interest in the formation of parametric images which model the kinetic behavior of each voxel individually. This approach is more appropriate when the volume cannot be effectively segmented into homogeneous regions that would be modeled with a single kinetic parameter set. Existing approaches to the creation of parametric images can be roughly categorized as "indirect," "semi-direct," and (our new method) "direct" [24] reconstruction.

Indirect methods work by first reconstructing the PET emission images for each of the K measurement times, and then estimating the kinetic parameters at each voxel. The primary difficulty of the indirect approach is that the low signal-to-noise ratio (SNR) of the time-activity curve (TAC) for each voxel makes accurate estimation of parameters difficult. To improve estimation accuracy, O'Sullivan *et al.* [25] applied ridge regression techniques to regularize the parameters using prior knowledge of their means and variances derived from the analysis of a reasonably large patient group. Huang *et al.* [26] applied a spatial smoothing step between the iterations of a nonlinear estimation process at each voxel. Later, Zhou *et al.* [27], [28] developed a two-stage algorithm whereby the kinetic parameters were estimated first using standard nonlinear techniques. In a second step the initial results were smoothed spatially and used to constrain the final estimates. (This method is further discussed in Section IV-B.) Kimura *et al.* [29] and Zhou *et al.* [30] have developed algorithms that cluster the images before estimation and regularize the data within the clusters.

Semi-direct algorithms, as they are sometimes named, attempt to improve the SNR by constraining the possible choices of time-courses for each voxel via signal sub-spaces or splines. Kao *et al.* [31] and Narayanan *et al.* [32] used principal component analysis (PCA) to decorrelate the sinograms in time. Similarly, Wernick *et al.* [33] applied PCA decomposition of PET data followed by reconstruction of tracer concentrations in the principal-component space. Nichols *et al.* [34], and Reutter *et al.* [35], [36] proposed reconstruction methods that use a b-spline specification of the time-activity curves. Kinetic parameters must then be estimated from the b-spline representation. It is important to note that spline-based methods have certain computational advantages when processing list mode data. However, the two-step process of first computing spline coefficients and then kinetic parameters still results in a loss of optimality, particularly if the number of spline coefficients is much larger than the number of kinetic parameters.

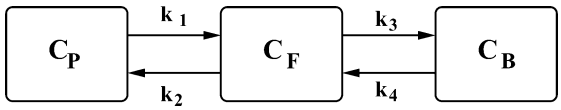

Fig. 2. Two-tissue compartment model with four kinetic parameters.

Ideally, one would like to estimate directly the space-domain kinetic parameters from the measured sinogram data. In fact, Carson and Lange [1] proposed direct estimation of kinetic parameters from PET data in 1985. In that paper, the authors outlined a general framework for a direct reconstruction algorithm based on expectation-maximization (EM) [37] iterations. Unfortunately, the Carson and Lange direct parametric reconstruction algorithm has never, to our knowledge, been fully implemented for nonlinear estimation of a dense set of voxels. Limber *et al.* [38] proposed an algorithm for direct parametric reconstruction using maximum likelihood (ML) estimation of kinetic parameters from PET data, but only demonstrated the algorithm for an 8×8 array of voxels. A number of authors have implemented direct nonlinear parameter estimation methods that were designed for segmented ROIs [39]–[44] rather than a dense set of voxels. In an alternative approach, Meikle *et al.* [45] first precomputed the time-activity curves for a range of possible nonlinear parameters and then directly reconstructed the linear weights for each of the nonlinear "basis" curves. Similarly, Matthews *et al.* [46] obtained predefined time-curves from other patients' reconstructions and used the EM algorithm to compute the weights of each curve. In other work, Carson [47] proposed an ML framework to estimate the ROI values from the projections, and Farncombe *et al.* [48] estimated organ uptake parameters that were incorporated into the reconstruction algorithm for dSPECT applications.

In this paper, we present an algorithm for direct nonlinear estimation of space-domain kinetic parameters in a dense volume of voxels. Our novel parametric reconstruction algorithm, which we call parametric iterative coordinate descent (PICD) [2], is in the spirit of Carson and Lange's method. However, PICD is a completely specified and implemented algorithm (see the Appendix) which we show to be computationally efficient with robust convergence properties. In fact, the computation required for parametric reconstruction using PICD is comparable to that required for more conventional maximum *a posteriori* (MAP) reconstruction of an image sequence from PET sinogram data. In other words, it is our claim that direct parametric reconstruction can have comparable computational requirements to indirect methods (recall that indirect methods require an initial reconstruction of all the data). The key to computational efficiency of the PICD method is the use of state

variables and nested optimization to decouple the nonlinearities of the forward tomographic model, the nonlinear kinetic model, and the Bayesian prior model. Notably, PICD is designed to compute the MAP estimate of the kinetic parameters using a prior distribution defined on any well-behaved transformation of the parameter space. This allows the regularization to be applied to the parameters that are deemed to be physiologically important. Simulation results, presented below, indicate that the PICD-generated parametric reconstructions have lower mean squared error and better visual quality than the best indirect methods.

Section II reviews the two-tissue compartment model and the set of ODEs that govern a tracer's kinetics. Section III introduces the PICD algorithm for direct parametric reconstruction and gives a detailed description of its implementation. Section IV first reviews some existing methods for image domain parameter estimation, and then suggests a useful method for regularization of pixel-wise approaches. Section V compares the computational complexity of the proposed methods. Section VI presents simulation results. Discussion and Conclusion follow the results.

II. Two-Tissue Compartment Model

In this paper, we used a two-tissue compartment model to describe the kinetic processes that are represented by the signal from each voxel of a reconstructed image. This model is commonly used to describe the uptake and retention of an analog of glucose, 2-deoxy-2-$[^{18}F]$ fluoro-D-glucose (FDG). The model can also be properly applied to receptor ligand studies provided that there is no nonspecific binding and that the tracer has been administered at sufficiently high specific activity. Fig. 2 illustrates the model: C_P (pmol/ml) is the molar concentration of tracer in the plasma, C_F (pmol/ml) is the molar concentration of unbound tracer, and C_B (pmol/ml) is the molar concentration of metabolized or bound tracer. The model depends on the kinetic parameters, k_1, k_2, k_3, and k_4, which specify the tracer exchange rates between compartments in units of inverse minutes. The parameters k_1, k_2, and k_4 are first-order rate constants, and k_3 is an *apparent* first-order rate constant describing a process (metabolism or receptor-binding) that proceeds in proportion to the concentration of the labeled tracer only, as long as the number of sites available for binding do not become rate-limiting.

In addition to the above-stated parameters, there are two compound parameter groups that have ready physiological interpretations and practical application, particularly for receptor-ligand imaging: binding potential (BP), and total volume of distribution (VD). BP is proportional to the number of receptors and VD represents the steady state distribution of tracer between the plasma and tissue. BP and VD can be expressed in terms of the aforementioned kinetic parameters

$$BP = \frac{k_3}{k_4} \tag{1}$$

$$VD = \frac{k_1}{k_2}\left(1 + \frac{k_3}{k_4}\right). \tag{2}$$

In applying the model in Fig. 2 to all voxels, we assume that the delivery of tracer is the same to all regions being imaged. In other words, the value of C_P is not a function of voxel position. However, the values of the kinetic parameters will be allowed to vary for each voxel location, s. Using these assumptions, the time variation of the concentrations for a single voxel are governed by the following ODEs:

$$\frac{dC_F(s,t)}{dt} = k_{1s}C_P(t) - (k_{2s} + k_{3s})C_F(s,t) + k_{4s}C_B(s,t) \tag{3}$$

$$\frac{dC_B(s,t)}{dt} = k_{3s}C_F(s,t) - k_{4s}C_B(s,t). \tag{4}$$

In this paper, $C_P(t)$ is assumed known. In practice, it can be measured directly from arterial plasma samples during the imaging procedure [6], or it may be estimated from imaged volumes that consist primarily of blood [49]–[53]. The solution to the ODEs in (3), (4) is given by

$$C_F(s,t) = \left\{ \frac{k_{1s}}{\alpha_2 - \alpha_1}\left[(k_{4s} - \alpha_1)e^{-\alpha_1 t} + (\alpha_2 - k_{4s})e^{-\alpha_2 t}\right] u(t) \right\} * C_P(t) \tag{5}$$

$$C_B(s,t) = \left\{ \frac{k_{1s}k_{3s}}{\alpha_2 - \alpha_1}[e^{-\alpha_1 t} - e^{-\alpha_2 t}]u(t) \right\} * C_P(t) \tag{6}$$

where $*$ indicates continuous-time convolution, α_1 and α_2 are real valued constants that result from the subtraction and addition of terms in (7) respectively, and $u(t)$ is the unit step function

$$\alpha_1, \alpha_2 = \frac{(k_{2s} + k_{3s} + k_{4s})}{2} \mp \frac{\sqrt{(k_{2s} + k_{3s} + k_{4s})^2 - 4k_{2s}k_{4s}}}{2}. \tag{7}$$

Next, we transform the kinetic parameters (k_1, k_2, k_3, k_4) to form the new parameters (a, b, c, d) as shown in Table I. This transformation is important because while the parameters (a, b, c, d) are well suited for optimization, (k_1, k_2, k_3, k_4) are physiologically more relevant. We use $\varphi_s = [a_s, b_s, c_s, d_s]^t$ to denote the parameter vector for each voxel s.

The total activity concentration (e.g., in nCi/ml) for voxel s at time t is denoted by

$$\begin{aligned} f(\varphi_s, t) &\triangleq (1 - V_B)\left[C_F(s,t) + C_B(s,t)\right] S_A e^{-\lambda t} + V_B C_{WB}(t) \\ &= (1 - V_B)\left[\left(a_s e^{-c_s t} + b_s e^{-d_s t}\right) u(t) * C_P(t)\right] \\ &\quad \times S_A e^{-\lambda t} + V_B C_{WB}(t) \end{aligned} \tag{8}$$

TABLE I
Forward and Inverse Transformations From Standard Kinetic Parameters $[k_{1s}, k_{2s}, k_{3s}, k_{4s}]$ for the Voxel s to New Parameters $[a_s, b_s, c_s, d_s]$. Note That $c_s = \alpha_2$ and $d_s = \alpha_1$ Given in (7)

Forward Transforms	Inverse Transforms
$a_s = \frac{k_{1s}}{2\Delta}(k_{2s} - k_{3s} - k_{4s} + \Delta)$	$k_{1s} = a_s + b_s$
$b_s = \frac{k_{1s}}{2\Delta}(-k_{2s} + k_{3s} + k_{4s} + \Delta)$	$k_{2s} = \frac{a_s c_s + b_s d_s}{a_s + b_s}$
$c_s = \frac{1}{2}(k_{2s} + k_{3s} + k_{4s} + \Delta)$	$k_{3s} = \frac{a_s b_s (c_s - d_s)^2}{(a_s + b_s)(a_s c_s + b_s d_s)}$
$d_s = \frac{1}{2}(k_{2s} + k_{3s} + k_{4s} - \Delta)$	$k_{4s} = \frac{c_s d_s (a_s + b_s)}{a_s c_s + b_s d_s}$
$\Delta = \lvert\sqrt{(k_{2s} + k_{3s} + k_{4s})^2 - 4k_{2s}k_{4s}}\rvert$	

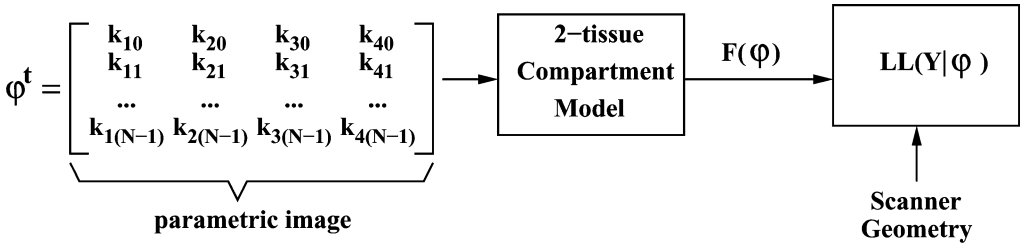

Fig. 3. Model used for direct parametric reconstruction of images.

where S_A is the initial specific activity of the tracer (nCi/pmol), λ is the decay rate of the isotope $(\min^{-1})$, V_B is a known constant for the volume fraction of the voxel that contains blood, and C_{WB} (nCi/ml) is the tracer activity concentration in whole blood (i.e., plasma plus blood cells plus other particulate matter).[1] We can simplify the expression for $f(\varphi_s, t)$ by defining the following functions:

$$\alpha(c_s, t) \triangleq \left\{C_P(t) * \left[e^{-c_s t}u(t)\right]\right\}(1 - V_B)S_A e^{-\lambda t} \quad (9)$$

$$\beta(d_s, t) \triangleq \left\{C_P(t) * \left[e^{-d_s t}u(t)\right]\right\}(1 - V_B)S_A e^{-\lambda t} \quad (10)$$

$$\gamma(t) \triangleq V_B C_{WB}(t). \quad (11)$$

With these definitions, $f(\varphi_s, t)$ can be written as

$$f(\varphi_s, t) = [a_s, b_s]\begin{bmatrix}\alpha(c_s, t)\\ \beta(d_s, t)\end{bmatrix} + \gamma(t). \quad (12)$$

We next define some vector and matrix notation that will be useful in discretization of the problem.[2] Let $t_0, \ldots, t_{K-1}$ be the K discrete times at which the tissue is imaged. Then, we may construct the vectors

$$\alpha(c_s) \triangleq [\alpha(c_s, t_0), \alpha(c_s, t_1), \ldots, \alpha(c_s, t_{K-1})] \quad (13)$$

$$\beta(d_s) \triangleq [\beta(d_s, t_0), \beta(d_s, t_1), \ldots, \beta(d_s, t_{K-1})] \quad (14)$$

$$\gamma \triangleq [\gamma(t_0), \gamma(t_1), \ldots, \gamma(t_{K-1})]. \quad (15)$$

Using this notation, the activity at each time for voxel s is given by the $1 \times K$ row vector

$$\begin{aligned} f(\varphi_s) &= [f(\varphi_s, t_0), f(\varphi_s, t_1), \ldots, f(\varphi_s, t_{K-1})] \\ &= [a_s, b_s]\begin{bmatrix}\alpha(c_s)\\ \beta(d_s)\end{bmatrix} + \gamma. \end{aligned} \quad (16)$$

Let the N voxels be indexed by the values $s = 0, 1, \ldots, N-1$, and let $\varphi = [\varphi_0, \varphi_1, \ldots, \varphi_{N-1}]$ denote the $4 \times N$ matrix of parameters at all voxels. With this, we define the $N \times K$ function

$$F(\varphi) = \begin{bmatrix} f(\varphi_0) \\ \vdots \\ f(\varphi_{N-1}) \end{bmatrix}$$

which maps the parametric image, φ, to the activity of each voxel at each time. Finally, let $F(\varphi, t_k)$ denote the kth column of $F(\varphi)$, so $F(\varphi, t_k)$ contains the activity for each voxel at time t_k.

[1]Notice that both $f(\varphi_s, t)$ and $C_{WB}(t)$ include the attenuation due to decay. Therefore, the sinogram data should not be decay corrected for the implementation of this method.

[2]This discretization approach is equivalent to interpreting the measured concentrations as representing instantaneous concentrations measured at midframe.

III. Parametric Reconstruction From Sinogram Data

In this section, we describe our method for directly reconstructing the parametric image, φ, from sinogram data. We will do this by first formulating a conventional scanner model under the assumption that the sinogram measurements are Poisson random variables. We will then use the kinetic model of Section II as the input to the scanner model as shown in Fig. 3. Once the complete forward model is formulated, we will present an iterative algorithm for computing the maximum *a posteriori* (MAP) estimate of the parametric image $\hat{\varphi}$ from the sinogram data. Once $\hat{\varphi}$ is computed, the activity images can be computed at any time t simply by evaluating $F(\varphi, t)$ using the kinetic model equations of (8).

A. Scanner Model

Let Y_{mk} denote the sinogram measurement for projection $0 \leq m < M$ and time frame $0 \leq k < K$, and let Y be the $M \times K$ matrix of independent Poisson random variables that form the sinogram measurements. Furthermore, let A be the forward projection matrix, with elements A_{ms} (counts-ml/nCi), and let μ be the number of accidental coincidences. Then the expected number of counts for each measurement at a given time, t_k is given by

$$E[Y_{mk}|F(\varphi, t_k)] = \sum_{s=0}^{N-1} A_{ms} f(\varphi_s, t_k) + \mu. \quad (17)$$

This relationship can be compactly expressed using matrix notation as

$$E[Y|F(\varphi)] = AF(\varphi) + \mu. \quad (18)$$

It is easily shown that under these assumptions the probability density for the sinogram matrix is given by [54]

$$p(Y|\varphi) = \prod_{k=0}^{K-1}\prod_{m=0}^{M-1} \frac{(A_{m*}F(\varphi, t_k) + \mu)^{Y_{mk}} e^{-(A_{m*}F(\varphi, t_k)+\mu)}}{Y_{mk}!} \quad (19)$$

where A_{m*} is the mth row of the system matrix, A. The log likelihood of the sinogram matrix is then given by

$$LL(Y|\varphi) = \sum_{k=0}^{K-1}\sum_{m=0}^{M-1} Y_{mk}\log(A_{m*}F(\varphi, t_k) + \mu) - (A_{m*}F(\varphi, t_k) + \mu) - \log(Y_{mk}!). \quad (20)$$

This is a very general formulation. For specific scanners, the form of the system matrix A may vary considerably, and accurate determination of the matrix A can be critical to obtaining accurate tomographic reconstructions [55], [56].

B. MAP Estimation Framework

We will use MAP estimation to reconstruct the parametric image. For this purpose, a cost function is formed by negating the log likelihood given in (20) and adding a stabilizing function

$$C(Y|\varphi) = -LL(Y|\varphi) + S(\varphi). \tag{21}$$

The MAP reconstruction, $\hat{\varphi}$, will be the parametric image that minimizes this cost function

$$\hat{\varphi} = \arg\min_{\varphi} C(Y|\varphi). \tag{22}$$

The stabilizing function can be obtained from an assumed prior probability distribution for the parametric image. In this work, we model the distribution of the parametric image as a Markov random field (MRF) with a Gibbs distribution of the form

$$p(\varphi) = \frac{1}{z}\exp\left\{-\sum_{\{s,r\}\in\mathcal{N}} g_{s-r}||T(\varphi_s) - T(\varphi_r)||_W^q\right\} \tag{23}$$

where z is the normalization constant, $\mathcal{N}$ is the set of all neighboring voxel pairs in φ, g_{s-r} is the coefficient linking voxels s and r, q is a constant parameter that controls the smoothness of the edges in the parametric image, $T(\cdot)$ is a transform function, and W is the diagonal weighting matrix.

In this paper, we will assume $q = 2$ and that $\mathcal{N}$ is formed with voxel pairs using an 8-point neighborhood system. In this case, the probability density function corresponds to a Gaussian Markov random field, and we choose the negative logarithm of this function as our stabilizing function

$$S(\varphi) = \sum_{\{s,r\}\in\mathcal{N}} g_{s-r}||T(\varphi_s) - T(\varphi_r)||_W^2. \tag{24}$$

By choosing an appropriate transform function, $T(\cdot)$, the regularization can be done in the space of the physiologically relevant parameters. Typically, we will select $T(\cdot)$ to transform from the a, b, c, d space to the k_1, k_2, k_3, k_4 as show in Table I; however, any well-behaved one-to-one transformation, $T(\cdot)$, is suitable for our algorithm.

C. Parametric Image Reconstruction Using PICD

The MAP reconstruction described in (22) is computed efficiently by an algorithm which we call parametric iterative coordinate descent (PICD). This algorithm is similar to the iterative coordinate descent (ICD) algorithm used in conventional PET image reconstruction [54], but it is adapted to account for the nonlinear parameters of the compartmental model. PICD sequentially updates the parameters of each voxel thereby monotonically decreasing the cost function given in (22). When $F(\varphi)$ is a nonlinear function, the PICD algorithm reduces computation by decoupling the dependencies between the compartment model nonlinearities and the forward tomography model.

In order to compute a PICD voxel update, we must compute

$$\varphi_s \leftarrow \arg\min_{\varphi_s} C(Y|\varphi_s). \tag{25}$$

To do this efficiently, we use the second-order Taylor expansion of the change in the cost function.

Suppose we are updating the parameters of voxel s from $\varphi_s = [a_s, b_s, c_s, d_s]^t$ to $\tilde{\varphi}_s = [\tilde{a}_s, \tilde{b}_s, \tilde{c}_s, \tilde{d}_s]^t$, and that we represent the change in the time response function of voxel s by the $1\times K$ vector function

$$\Delta f(\tilde{\varphi}_s, \varphi_s) = f(\tilde{\varphi}_s) - f(\varphi_s).$$

We next define a simplified cost functional

$$\Delta C(\tilde{\varphi}_s, \varphi_s) = -LL(Y|\tilde{\varphi}_s) + LL(Y|\varphi_s) + \sum_{r\in\partial s} g_{s-r}||T(\tilde{\varphi}_s) - T(\varphi_r)||_W^2. \tag{26}$$

Notice that since $\Delta C(\tilde{\varphi}_s, \varphi_s)$ is equal to the change in the cost functional $C(Y|\tilde{\varphi}_s)$ within a constant, so it may be used to compute the voxel update of (25). The value of $\Delta C(\tilde{\varphi}_s, \varphi_s)$ can then be locally approximated with a second-order Taylor series as

$$\Delta C(\tilde{\varphi}_s, \varphi_s) \approx \Delta f(\tilde{\varphi}_s, \varphi_s)\theta_1 + \frac{1}{2}||\Delta f(\tilde{\varphi}_s, \varphi_s)||_{\theta_2}^2 + \sum_{r\in\partial s} g_{s-r}||T(\tilde{\varphi}_s) - T(\varphi_r)||_W^2 \tag{27}$$

where ∂s denotes the set of voxels that are 8-neighbors of voxel s, θ_1 is a $K\times 1$ vector, θ_2 is a $K\times K$ diagonal matrix, and $||x||_{\theta_2}^2 = x^t\theta_2 x$. Here, the values of θ_1 and θ_2 consist of the first and second derivatives respectively of the log likelihood function evaluated at each time frame. These derivatives at time frame k can be iteratively updated using the equations of the conventional ICD algorithm [54], given in (28) and (29).

$$[\theta_1]_k \leftarrow \sum_{m=0}^{M-1} A_{ms}\left(1 - \frac{Y_{mk}}{A_{m*}F(\varphi, t_k) + \mu}\right) \tag{28}$$

$$[\theta_2]_{k,k} \leftarrow \sum_{m=0}^{M-1} Y_{mk}\left(\frac{A_{ms}}{A_{m*}F(\varphi, t_k) + \mu}\right)^2. \tag{29}$$

Using the notation defined in (13)–(15), the PICD update can then be expressed as

$$\tilde{\varphi}_s \leftarrow \arg\min_{\tilde{\varphi}_s}\left\{\Delta f(\tilde{\varphi}_s, \varphi_s)\theta_1 + \frac{1}{2}||\Delta f(\tilde{\varphi}_s, \varphi_s)||_{\theta_2}^2 + \sum_{r\in\partial s} g_{s-r}||T(\tilde{\varphi}_s) - T(\varphi_r)||_W^2\right\} \tag{30}$$

where

$$\Delta f(\tilde{\varphi}_s, \varphi_s) = [\tilde{a}_s, \tilde{b}_s]\begin{bmatrix}\alpha(\tilde{c}_s)\\ \beta(\tilde{d}_s)\end{bmatrix} - [a_s, b_s]\begin{bmatrix}\alpha(c_s)\\ \beta(d_s)\end{bmatrix}. \tag{31}$$

We have found that the PICD update is best implemented using two-stage nested optimization shown in (32) at the bottom of the

$$(c_s, d_s) \leftarrow \arg\min_{\tilde{c}_s\geq\tilde{d}_s\geq 0}\left\{\arg\min_{\tilde{a}_s,\tilde{b}_s\geq 0}\left\{\Delta C([\tilde{a}_s, \tilde{b}_s, \tilde{c}_s, \tilde{d}_s], \varphi_s)\right\}\right\} \tag{32}$$

previous page. This nested optimization strategy is very important in reducing computation and assuring robust convergence. The inner optimization over $\tilde{a}_s$ and $\tilde{b}_s$ must be performed many times since this result is required for each update of outer optimization over $\tilde{c}_s$ and $\tilde{d}_s$. Fortunately, optimization over $\tilde{a}_s$ and $\tilde{b}_s$ can be done very efficiently with a simple steepest descent algorithm because this optimization does not require updating of θ_1, θ_2, $\alpha(\tilde{c}_s)$, or $\beta(\tilde{d}_s)$. Optimization with respect to $(\tilde{c}_s, \tilde{d}_s)$ is done using iterative one-dimensional golden section search along the $\tilde{c}_s$ and $\tilde{c}_s + \tilde{d}_s$ directions. This method assures the convergence is to a local minimum that meets the Kuhn–Tucker conditions [57]. The Appendix contains pseudocode that specify details of the algorithm.

D. Multiresolution Initialization

It is well known that for the tomographic problem the ICD reconstruction algorithm tends to have slow convergence at low spatial frequencies [58]. Normally, this problem is solved by initializing the ICD iterations with a FBP reconstruction. In this case, most of the residual error is only at high frequencies, so the ICD iterations converge quickly. However, for parametric reconstruction there is no simple direct reconstruction algorithm, such as FBP, to use as an initialization for the PICD iterations.

To solve this problem, we use a multiresolution reconstruction scheme, which first computes coarse resolution reconstructions and then and proceeds to finer scales. The coarsest resolution reconstruction is initialized with a single set of parameters obtained by weighted least squares curve fitting to the average emission rate of each time frame. Importantly, the average activity of each time frame can be calculated directly from the sinogram data with little computation. Finer resolution reconstructions are then initialized by interpolating the parametric reconstruction of the previous coarser resolution. This recursive process reduces computation because the computationally inexpensive reconstructions at coarse levels provide a good initialization for finer resolution reconstructions.

IV. Image Domain Parameter Estimation Methods

For purposes of comparison, we will also consider image domain methods which estimate parameters at each voxel from reconstructed images at each time. Each of these methods requires that the sinogram at each time frame be reconstructed using conventional reconstruction methods. For these methods, let $x_s(t_k)$ denote the reconstructed activity of voxel s at time frame k collected at time t_k, and let

$$x_s = [x_s(t_0), x_s(t_1), \ldots, x_s(t_{K-1})]$$

denote the activity of voxel s at all time frames.

A. Pixel-Wise Weighted Least Square (PWLS) Method

The pixel-wise weighted least squares method estimates the parameters of each voxel by iteratively minimizing the weighted square error between the reconstructed time response of the voxel and the model output.

The parameters of voxel s are estimated as

$$\hat{\varphi}_s = \arg\min_{\varphi_s} \|x_s - f(\varphi_s)\|^2_{W_s} \tag{33}$$

where W_s is the $K \times K$ diagonal weighting matrix for voxel s. The weight of each time frame is chosen to be inversely proportional to the variance of the voxel activity in that time frame. This variance can be approximated by the activity estimate of this voxel, normalized by the duration of the time frame. In this case, W_s is a diagonal matrix with diagonal elements given by

$$[W_s]_{k,k} = \frac{\Delta t_k}{\max\{x_{\text{MIN}}, x_s(t_k)\}} \tag{34}$$

where Δt_k is the duration of time frame k, and x_{MIN} controls the maximum allowable value for the weights.

The parameters are estimated using the same nested optimization strategy as specified in (32). In fact, this algorithm differs from the parametric reconstruction in only two respects. First, the data derivatives of (28) and (29) are replaced by

$$\theta_1 = -2W_s(x_s - f(\varphi_s)) \tag{35}$$

$$\theta_2 = 2W_s; \tag{36}$$

and second, the stabilizing functional $S(\varphi)$ is set to 0.

B. Pixel-Wise Weighted Least Square Method With Spatial Regularization

The spatial variation of the PWLS parameter estimates can be reduced by adding a stabilizing function to (33). The resulting estimate is given by

$$\hat{\varphi} = \arg\min_{\varphi} \sum_{s=0}^{N-1} \|x_s - f(\varphi_s)\|^2_{W_s} + S(\varphi) \tag{37}$$

where $S(\cdot)$ is the spatial stabilizing functional [25], [26].

In the first method, which we call the pixel-wise least squares regularized (PWLSR) method, the stabilizing function has the form specified in (24). This is the same stabilizing function as was used for direct parametric reconstruction.

For the second method, which we call the PWLSZ method, we implemented the stabilizing functional described in [26]. This method smooths the PWLS estimate and uses it in the stabilizing function. Let $H(\cdot)$ be a smoothing operator and φ^P be the PWLS parameter estimate. The constrained parametric image is then given by

$$\varphi^C = H(\varphi^P).$$

Next, a weight is calculated for each voxel. For voxel s the corresponding weight is

$$w_s = \frac{\left\|x_s - f(\varphi^P)\right\|^2_{W_s}}{\left(\varphi^P_s - \varphi^C_s\right)^2}.$$

Using the constraint images and weights, the stabilizing function is given by

$$S(\varphi) = \sum_{s=0}^{N-1} w_s \left(\varphi_s - \varphi^C_s\right)^2. \tag{38}$$

Notice that the stabilizing function of (38) penalizes the difference between the parameters and a smoothed version of the parameters. Alternatively, the more traditional stabilizing function of (24) penalizes the spatial derivatives of the parameters.

TABLE II
COMPUTATIONAL COMPLEXITY FOR A SINGLE FULL ITERATION OF PICD, PWLS, PWLSR, AND ICD

Algorithm	Function	Per Iteration Complexity
PICD	Direct parametric reconstruction	$KN(L_{cd}L_{ab} + K_cL_{cd} + M_0)$
PWLS	Parameter estimation from reconstruction	$KN(L_{cd}L_{ab} + K_cL_{cd})$
PWLSR/PWLSZ	Regularized parameter estimation from reconstruction	$KN(L_{cd}L_{ab} + K_cL_{cd})$
ICD	MAP image reconstruction	$KN(M_0)$

Notation: N = number of voxels; M_0 = is average number of projections per voxel; K = is the number of time frames; K_c = number of time points in the time-convolution kernel; L_{ab} = number iterations required for each update of $(\bar{a}, \bar{b})$; L_{cd} = number iterations required for each update of $(\bar{c}, \bar{d})$. Expressions do not include the computational cost of regularization.

For both of these methods the solution to (37) is computed using the nested optimization strategy specified in (32) and the data derivatives specified in (35) and (36).

C. Linear (Logan) Method

Kinetic parameter groups can sometimes be easily estimated by properly transforming the data. The Logan plot is a popular integral transform of the model given in (3), (4), and (8). This transformation can be expressed as follows:

$$\left[\frac{\int_0^{t_k} x_s(t)dt}{x_s(t_k)}\right] = \frac{k_{1s}}{k_{2s}}\left(1 + \frac{k_{3s}}{k_{4s}}\right)\left[\frac{\int_0^{t_k} C_P(t)dt}{x_s(t_k)}\right] + const. \tag{39}$$

When the transformed variables (quantities in square brackets above) are plotted against each other, the resulting line has a slope equal to the compound parameter VD_s which is defined in (2).

To calculate BP_s the brain is segmented into a target region and a reference region. The target region consists of voxels within the brain that contain receptors for the tracer; and the reference region consists of the voxels that do not contain receptors for the tracer (i.e., $k_3 = 0$). Let, $\mathcal{T}$ be the set of voxel indexes from target region, and $\mathcal{R}$ be the set of voxel indexes from reference region.

For a voxel $r \in \mathcal{R}$ (from reference region), the distribution volume is

$$VD_r = \frac{k_{1r}}{k_{2r}}, \quad r \in \mathcal{R}.$$

For each voxel $s \in \mathcal{T}$ (from target region), the distribution volume ratio (DVR_s) is

$$\begin{aligned} DVR_s &= \frac{VD_s}{\frac{1}{|\mathcal{R}|}\sum_{r\in\mathcal{R}} VD_r} \\ &= 1 + \frac{k_{3s}}{k_{4s}} \end{aligned} \tag{40}$$

where $|\mathcal{R}|$ denotes the number of voxels in the region $\mathcal{R}$. Hence, the binding potential for the target region can be calculated as $BP_s = DVR_s - 1$.

The assumptions that are used in the derivation of (39) and (40) are as follows.

- k_1/k_2 ratio is constant for every voxel in the brain (i.e., both target and referenced regions).
- The tracer has high specific activity (so binding can be described as an apparent first-order process).

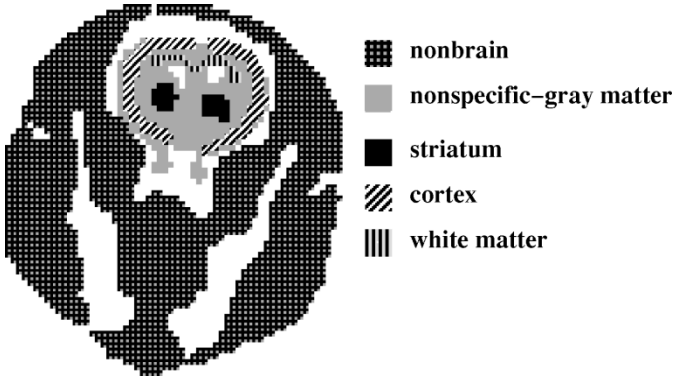

Fig. 4. Single-slice rat phantom. Regions of the rat phantom were derived from a segmented MR image. Different fill patterns indicate kinetically distinct tissue regions. Striatum is a region containing specific receptors for the tracer. Nonspecific-gray matter is tissue containing no specific binding sites for tracer but comparable blood flow parameters (k_1, k_2) to striatal area; cortex is modeled as containing low concentration of binding sites; white matter in our dynamic phantom contains no specific binding sites and low flow; non-brain, which comprises much of the slice has fast influx and efflux of tracer. Solid white areas in figure represent a mixture of background regions that do not contain any activity over time. The small white areas dorsal to (above) the striatum are ventricles that contain cerebral spinal fluid and no tracer. White areas surrounding brain correspond to skull which does not take up appreciable amounts of tracer.

- Blood volume fraction, V_B, is zero inside the target and the reference.
- $k_3 = 0$ for all the voxels in the reference region.

V. COMPUTATIONAL COMPLEXITY ANALYSIS

In order to better understand the computational requirements of parametric reconstruction, we derive expressions for the computational complexity of a number of parameter estimation algorithms.

First, consider the PICD algorithm. For each voxel update, the data derivatives, θ_1 and θ_2, are computed once. The complexity of this computation is $\mathcal{O}(KM_0)$, where K is the number of time frames, and M_0 is the average number of nonzero projections per voxel. Assume the nested search described in (32) requires L_{cd} evaluations of nonlinear parameters $\tilde{c}_s$ and $\tilde{d}_s$. Furthermore, assume that each update of $\tilde{c}_s$ or $\tilde{d}_s$ requires L_{ab} evaluations of linear parameters $\tilde{a}_s$ and $\tilde{b}_s$.

Each evaluation with respect to $\tilde{c}_s$ or $\tilde{d}_s$ requires a convolution with the plasma input function and L_{ab} evaluations with respect to $\tilde{a}_s$ and $\tilde{b}_s$. Let K_c be the number of time points in the time-convolution kernel. Then the convolution requires $\mathcal{O}(K_cK)$ operations, and the evaluation with respect to $\tilde{a}_s$ and $\tilde{b}_s$ requires $\mathcal{O}(K)$ operations; so the total complexity of a voxel

TABLE III
KINETIC PARAMETERS USED IN THE SIMULATIONS FOR DISTINCT TISSUE REGIONS OF THE RAT HEAD

Region	k_1 min^{-1}	k_2 min^{-1}	k_3 min^{-1}	k_4 min^{-1}	a min^{-1}	b min^{-1}	c min^{-1}	d min^{-1}
Background	0	0	0	0	0	0	0	0
CSF	0	0	0	0	0	0	0	0
Nonbrain	.1836	.8968	0	0	.1836	0	.8968	0
Nonspecific-gray matter	.0918	.4484	0	0	.0918	0	.4484	0
Striatum	.0918	.4484	1.2408	.1363	.02164	.07016	1.7914	.0312
Cortex	.0918	.4484	.141	.1363	.0607	.0311	.628	.09725
White matter	.02295	.4484	0	0	.02295	0	.4484	0

update is given by $\mathcal{O}(KM_0 + L_{cd}(K_cK + L_{ab}K))$, and the total complexity of PICD per full iteration for an N voxel image is given by $\mathcal{O}(KN(L_{cd}L_{ab} + K_cL_{cd} + M_0))$. The complexity of PWLS, PWLSR, and ICD, given in Table II, are then derived by removing the terms corresponding to operations that are not performed.

VI. SIMULATIONS

Sections VI-A–VI-C compares the accuracy and computational burden of direct parametric reconstruction and image domain estimation methods.

A. Phantom Design

Our simulation experiments are based on a phantom of a rat's head. Fig. 4 shows a schematic representation of the rat phantom and its constituent regions. The phantom has 7 regions including the background. These regions were obtained by segmenting an MRI scan of a rat through automated and manual techniques [59]. The regions and their corresponding parameters [60] are given in Table III, and their time activity curves are shown in Fig. 5. Time frames of emission images are generated using these parameter images and the two-tissue compartment model equations, and the plasma function, $C_P(t)$, is generated using (2) from [53]. In order to achieve sufficient accuracy, the convolution is implemented with $K_c = 691$ sample points. The blood contribution to the PET activity is assumed to be zero, and the tracer is assumed to be raclopride with ^{11}C, which has a decay constant of $\lambda = 0.034\ \mathrm{min}^{-1}$. Total scan time is 60 min., divided into 18 time frames with 4×0.5 min, 4×2 min, and 10×5 min. The phantom had a resolution of 128×128 with each voxel having dimensions of $(1.2\ \mathrm{mm})^3$.

The rat phantom image at each time frame is forward projected into a sinogram using a Poisson model for the detected counts with a background (accidental coincidence) level of $\mu = 0.001$. Each sinogram consists of 180 angles and 200 radial bins per angle. This results in a value of $M_0 \simeq 934$. A triangular point spread function with a 4 mm base width is used in forward projections. The blood function, $C_P(t)$ is scaled so that the total number of counts in all sinogram frames is approximately 10 million.

B. Algorithm Implementation

Direct reconstructions were computed using the PICD algorithm with three levels of multiresolution optimization corresponding to resolutions of 32×32, 64×64 and 128×128. The reconstructions used $L_{cd} \simeq 35$ and $L_{ab} = 15$. In most cases,

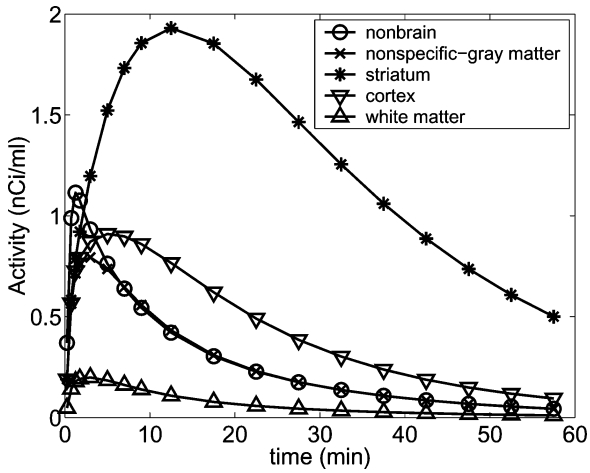

Fig. 5. Time-activity curves for five distinct tissue regions in rat brain phantom.

regularization was applied directly to the k_1, k_2, k_3, and k_4 parameters; so the stabilizing functional had the form

$$S(k_1, k_2, k_3, k_4) = \sum_{i=1}^{4} \frac{1}{2\sigma_{k_i}^2} \sum_{\{s,r\} \in \mathcal{N}} g_{s-r} |k_{i,s} - k_{i,r}|^2 \quad (41)$$

where the function g_{s-r} is inversely proportional to the distance between the voxels s and r and normalized to sum to 1, and the constants $\sigma_{k_i}^2$ control the regularization for each of the four parameters. The maximum likelihood (ML) estimate of $\sigma_{k_i}^2$ was computed for each parameter from the original parametric image using the formula [61]

$$\hat{\sigma}_{k_i}^2 = \frac{1}{N} \sum_{\{s,r\} \in \mathcal{N}} g_{s-r} |k_{i,s} - k_{i,r}|^2. \quad (42)$$

In the original formula, N is the number of voxels in the image; however some parameter images have very few nonzero voxels, so we choose N to be the number of nonzero voxels in the image. These ML parameters are then linearly scaled all together to find a set of regularization parameters that minimize the RMSE of the estimated kinetic parameters. The resulting diagonal weighting matrix, W, from (24) has diagonal entries given by $W_{i,i} = \beta\left(1/2\sigma_{k_i}^2\right)$ where β is the scaling factor that minimizes the parameter RMSE. Some results use regularization in the k_1, k_2, BP, and VD parameters. In this case, scaling parameters are selected similarly using the appropriate parameter values.

The image domain parameter estimation methods of Section IV require that the image be reconstructed for each time

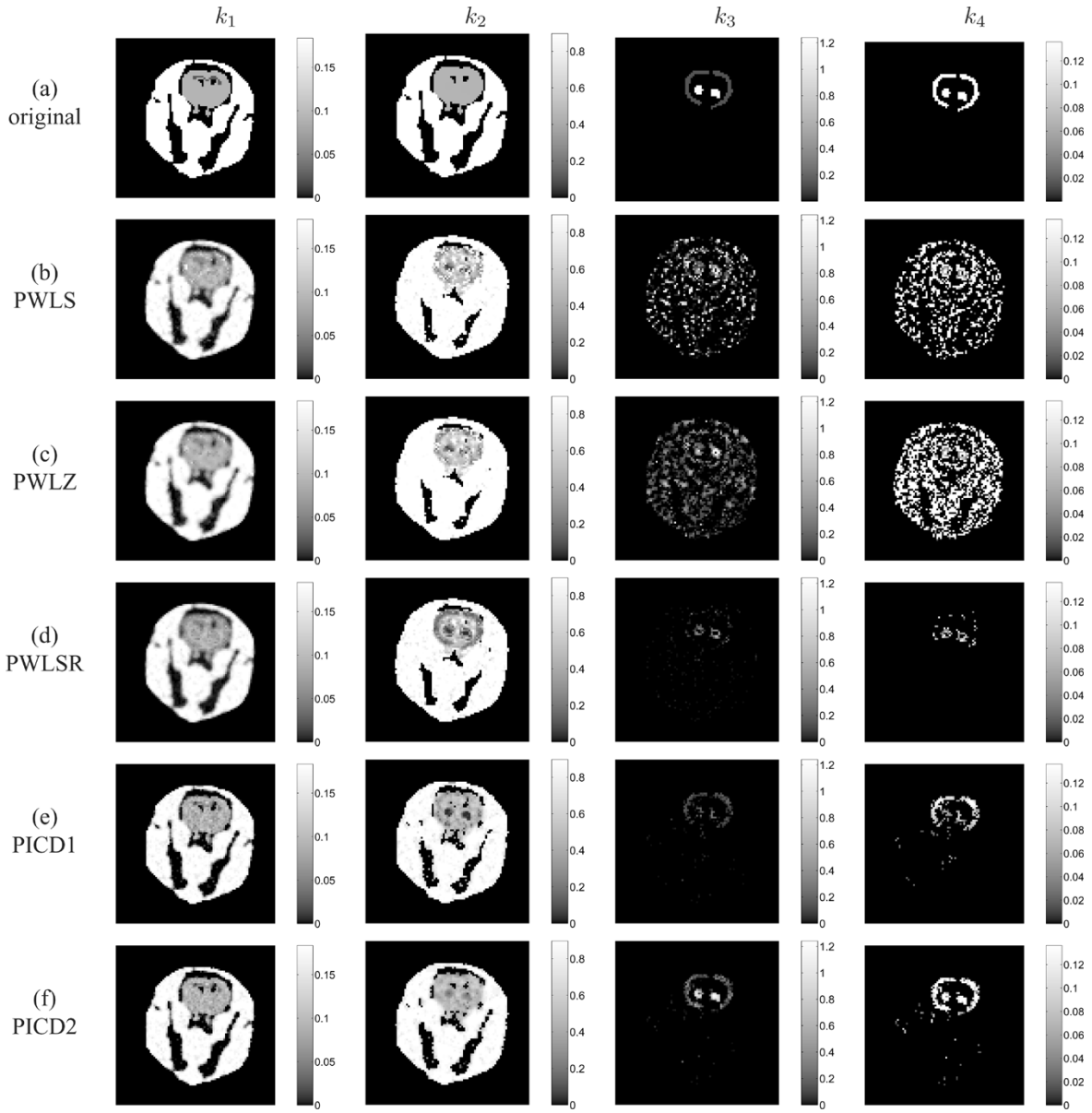

Fig. 6. Parametric images of k_1, k_2, k_3 and k_4 estimated by the algorithms; (a) original (b) PWLS (c) PWLSZ (d) PWLSR (e) PICD1: PICD reconstruction (new method) regularized on k_1, k_2, k_3, and k_4 (f) PICD2: PICD reconstruction (new method) regularized on k_1, k_2, BP, and VD.

frame. For this purpose, we used MAP image reconstruction with a quadratic prior (41) and a single fixed regularization parameter for all frame times. This single fixed parameter was chosen to minimize the total mean square error of the reconstructed emission image frames. The weighting matrix required for the PWLS, PWLSZ, and PWLSR algorithms was computed using (34) with $x_{\mathrm{MIN}} = 0.05\,\mathrm{nCi/ml}$.

In order to compute the PWLSZ reconstruction as described in Section IV-B, we smoothed the result of PWLS reconstruction with a 3×3 equal weight filter to calculate the constraints and weights. The weights were then scaled to minimize the MSE of the parameter estimates.

The PWLSR method was computed using a prior model on the k_1, k_2, k_3, and k_4 parameters in a manner similar to that used for parametric reconstruction. As with parametric reconstruction, the $\sigma^2_{k_i}$ constants were first selected using the ML estimation method described above, and then scaled to yield the minimum RMSE estimates of the parameters.

For the linear (Logan) method, the cortex and striatum regions are selected as target regions, and the nonspecific-gray matter was used as the reference region. Since these regions were selected precisely from simulated data, all assumptions of this method are perfectly satisfied.

A fixed number of iterations is used for each method. The multiresolution PICD method uses 30 iterations at 32×32 resolution, 20 iterations at 64×64 resolution, and 20 iterations at 128×128 resolution. Image domain methods use 15 iterations.

C. Results

Fig. 6 shows the reconstructions of the kinetic parameters. The first row contains the original parametric images. The remaining rows are respectively the reconstructions of PWLS,

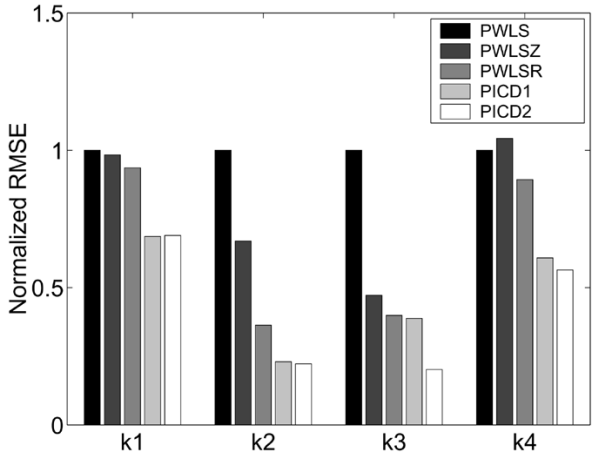

Fig. 7. Normalized RMSE for the reconstructed parametric images. PICD1 denotes the PICD reconstruction regularized on k_1, k_2, k_3, and k_4. PICD2 denotes the PICD reconstruction regularized on k_1, k_2, BP, and VD. Notice that PICD2 produces the lowest RMSE.

PWLSZ, PWLSR, PICD reconstruction regularized on k_1, k_2, k_3, and k_4, and PICD reconstruction regularized on k_1, k_2, BP, and VD.[3] In addition, the normalized RMSE of parameters k_1, k_2, k_3, and k_4 estimated by these algorithms are listed in Fig. 7. The normalized RMSE of a parameter is computed as

$$\text{normalized RMSE}(k_i) = \frac{\sqrt{\frac{1}{|\mathcal{S}|}\sum_{s\in\mathcal{S}}\left(k_{i,s}^{\text{true}} - k_{i,s}^{\text{estimated}}\right)^2}}{\sqrt{\frac{1}{|\mathcal{S}|}\sum_{s\in\mathcal{S}}\left(k_{i,s}^{\text{true}} - k_{i,s}^{\text{PWLS}}\right)^2}}$$

where $\mathcal{S}$ is the domain where RMSE is computed, $|\mathcal{S}|$ is the number of voxels in this domain, $k_{i,s}^{\text{true}}$ is the original value, $k_{i,s}^{\text{PWLS}}$ is the PWLS estimate of the parameter, and $k_{i,s}^{\text{estimated}}$ is the estimated value of the parameter for voxel s. The RMSE of k_1 is calculated over the whole image. The RMSE of parameters k_2 and k_3 are calculated over the support of k_1, and the RMSE of k_4 is calculated over the support of k_3.[4]

For the nonlinear parameters k_3 and k_4, the PWLS and PWLSZ methods both produced reconstructions which are very noisy, and this is reflected in the RMSE calculations. The PWLSR method with the GMRF prior produces lower RMSE reconstructions with more visually acceptable results for k_3 and k_4; however some details in these nonlinear parameters are lost. The parametric reconstruction regularized on k_1, k_2, k_3, and k_4 produces higher SNR reconstructions than any of the image domain methods, and the reconstructed images are visually similar to the original phantom. However, the parametric reconstructions with regularization on k_1, k_2, BP, and VD yield the best quality results judging from both the visual quality and the computed RMSE.

For the comparison of parameters BP and VD, spatial regularization is applied on k_1, k_2, BP, and VD. In this case, the scaling of the four regularization constants are chosen to minimize the RMSE of the BP and VD estimates alone. The results are shown in Fig. 8 and the normalized RMSE of the estimates of all methods are given in Fig. 9. The RMSE of BP is estimated over the support of k_3, and the RMSE of VD is estimated over the support of k_1. Again, parametric image reconstruction produces the lowest RMSE estimation for both BP and VD.

Once the parametric image is reconstructed, the ODEs can be solved for any particular time to reconstruct the corresponding emission image. Fig. 10 compares these reconstructions to the conventional reconstructions computed using FBP and MAP reconstruction for time frames 5, 10, and 15. The FBP reconstructions use a Hamming filter with cutoff at the Nyquist frequency. The RMSE of these reconstructions for each frame and for total RMSE of all frames are given in Fig. 11.

Finally, the convergence speed as a function of CPU time for all algorithms is given in Fig. 12. The time needed to reconstruct emission images required by image domain methods is included in this figure. As can be seen from this figure, the convergence speed of direct parametric reconstruction is comparable to the pixel-wise methods. It has been shown that ICD has more rapid convergence at high spatial frequencies and relatively slower convergence at low spatial frequencies [58]. Therefore, we used multiresolution initialization to speed the convergence of lower frequency components in the parametric image. Table IV lists the CPU time required for a single iteration of each method. Notice that direct parametric reconstruction using PICD does not require substantially more computation per iteration than the image domain methods, and the image domain methods require that the images first be reconstructed. This result is consistent with the complexity listed in Table II since in this example, $(K_c L_{cd} = 24{,}185) \gg (M_0 = 934) \gg (L_{cd} L_{ab} = 525)$; so the computational complexity of the time convolution required for kinetic parameter estimation dominates the computations required for the tomographic reconstruction.

VII. Discussion

In Section VI-C, we demonstrated that the kinetic parameters estimated by the direct parametric image reconstruction (ie. the "direct") have lower overall error as compared to those estimated in the image domain (i.e., the "indirect"). The improvement in the visual quality and the error of the kinetic parameter estimation may be due to the following factors.

- All the available data are used simultaneously.
- Kinetic parameters are estimated directly from PET sinogram data (for which we have a very good error model).
- Nonlinear estimation methods are used (so there is no need to linearize the model and introduce unwanted inaccuracy).
- Spatial regularization is done in the kinetic parameter domain (because neighboring voxels probably have similar *function*).

In contrast, the various image domain methods (described in Section IV) depend on the quality of the tomographic reconstructions of time-activity curves. FBP is still commonly used to reconstruct the dynamic PET data; unfortunately, it cannot produce the quality and the resolution achieved by the iterative reconstruction techniques. Iterative methods (e.g., EM, ordered

[3]A very small amount of regularization was also used for k_3 and k_4 (i.e., $\sigma_{k_3}^2 = 1\ \text{min}^{-2}$ $\sigma_{k_4}^2 = 0.1\ \text{min}^{-2}$) to suppress impulsive noise in these reconstructions.

[4]When k_1 is zero, then k_2 and k_3 are not defined. Similarly, when k_3 is zero, k_4 is not defined.

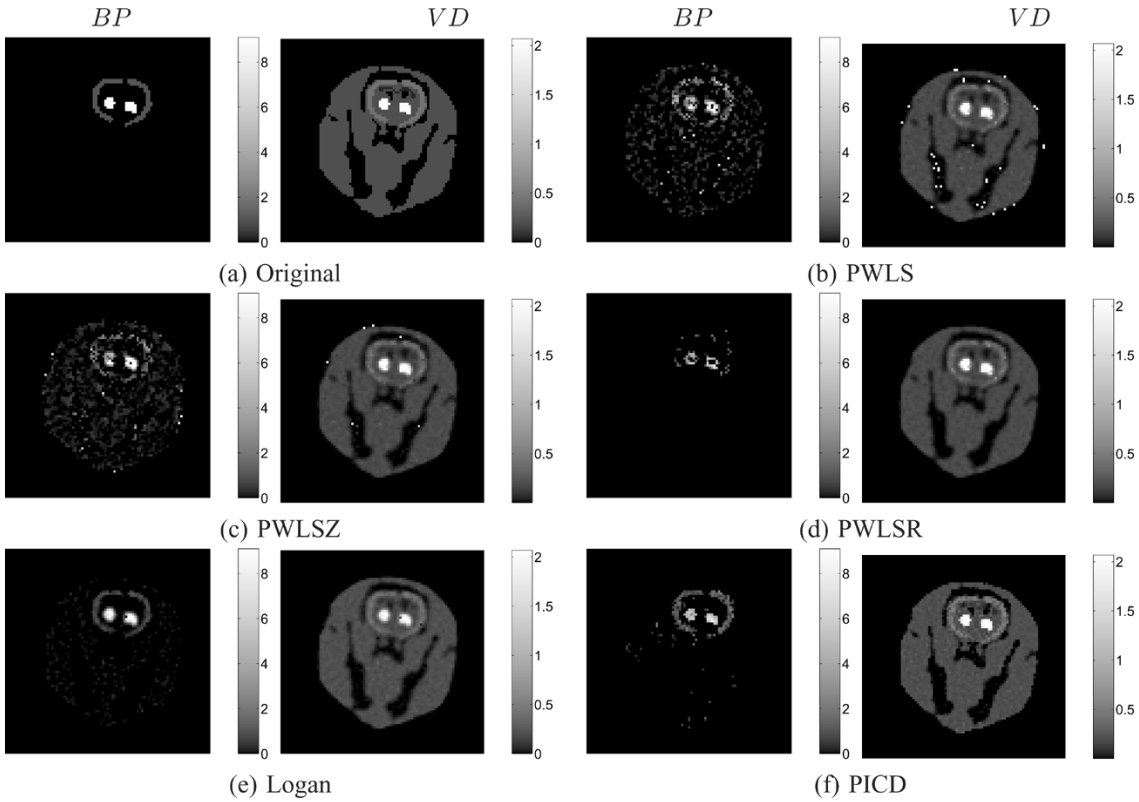

Fig. 8. Parametric images of BP and VD estimated by the algorithms; a) original; (b) PWLS; (c) PWLSZ; (d) PWLSR; (e) Logan; (f) PICD reconstruction (new method).

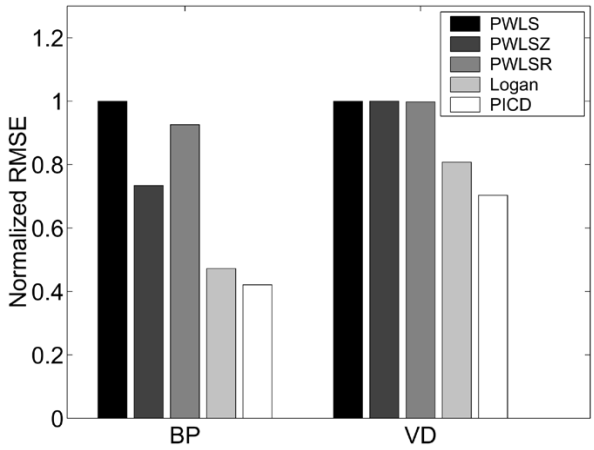

Fig. 9. Normalized RMSE for the reconstructed BP and VD. PICD reconstruction uses regularization on k_1, k_2, BP, and VD. Notice that PICD reconstruction gives the lowest RMSE results.

subset EM [62], or MAP [54]) require that images be reconstructed for each time frame and each slice. Therefore, direct parametric reconstruction reduces the dimensionality of the estimation problem from the number of time frames to the number of kinetic parameters in the compartment model. In our simulations, the dimensionality of the estimation problem was reduced by a factor of 4.5 (from 18 time frames to four parameters) by the direct method.

When using an image domain approach, spatial regularization can reduce the high spatial variance in the parametric images. We have found that spatial regularization based on a Gaussian Markov model produces less estimation error for all kinetic parameters except BP, compared with a smoothing filter-based constraint.

The linear (Logan plot) method described in Section IV-C is a very fast estimation technique. It tends to produce smooth images because it involves an integral transform of the data which suppresses noise. However, this method can only estimate some of the (compound) kinetic parameters. In receptor-ligand imaging, it provides no means for estimating k_1, k_2, k_3, or k_4, individually. Furthermore, to derive BP from distribution volume ratio, there must exist a reference region in the brain devoid of receptors ($k_3 = 0$). For some tracers (e.g., muscarinic or nicotinic ligands), there is no readily apparent reference region and so the value of the Logan method is compromised. Even when an appropriate reference region exists in theory (e.g., for dopaminergic ligands) the validity of the parameter estimates in the rest of the tissue can be biased by the placement of (or spillover of activity into) the reference ROI. In our simulations, we use the precise target (striatum and cortex) and reference (nonspecific-gray matter) regions for this method which are selected from the original image.

Another drawback to linearizations of the model is that they achieve some of their computational simplicity by unmet model assumptions (e.g., that the blood volume fraction in the reference and target tissues is zero over all time). These simplifications have been shown to introduce biases that are aggravated with decreasing SNR [63]–[65]. Another common assumption that is implicit in the use of Logan-plot methods is that the k_1/k_2 ratio everywhere in the brain is constant (although we

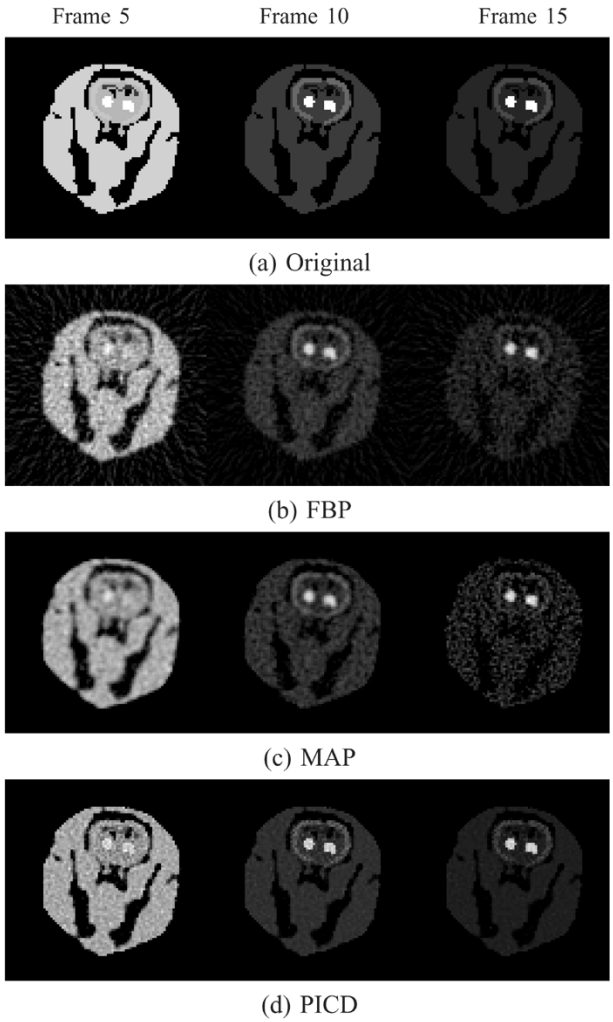

Fig. 10. Activity images. (a) Original phantom, (b) FBP reconstruction, (c) MAP, and (d) PICD reconstruction (new method) for frames 5, 10, and 15.

TABLE IV
CPU TIME FOR A SINGLE ITERATION

Method	time for 1 iteration (sec.)
PWLS	474
PWLSZ	487
PWLSR	526
PICD	594

satisfy this constraint in our simulated data, the direct estimation method does not require it). This ratio can, of course, be regularized spatially in the direct method. Local regularization, however, is not nearly as rigid a requirement as expecting k_1/k_2 to be constant everywhere.

Although direct parameter estimation from the PET sinograms has been proposed previously as the EMPIRA algorithm [1], this or equivalent methods have not been fully implemented. This is likely due to the computational complexity of the M-step which was not fully specified, and the slow convergence of conventional EM iterations. With the development of computationally efficient and rapidly converging methods such as have been demonstrated in this paper, direct reconstruction to parametric images should become widely applied to dynamic

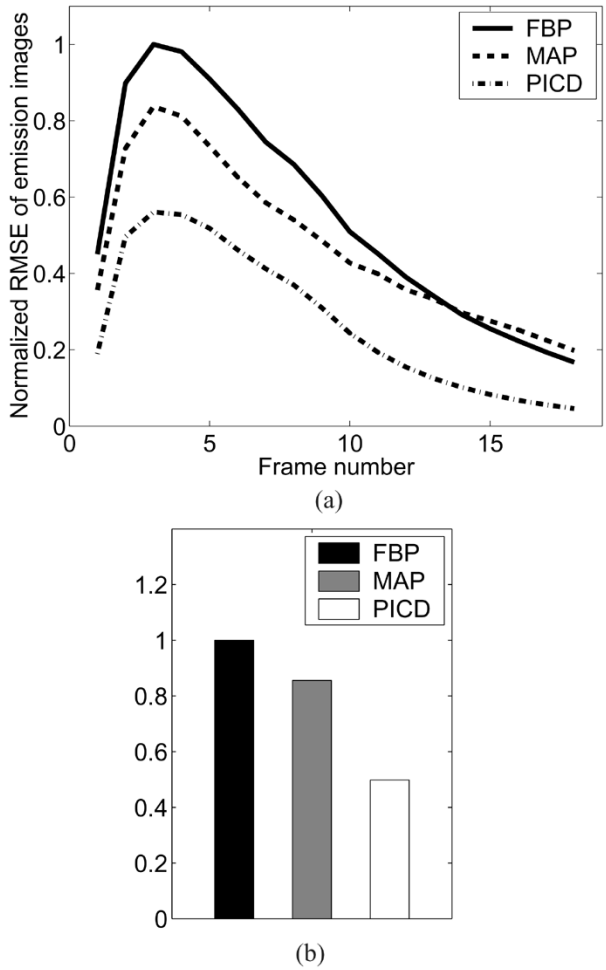

Fig. 11. Normalized RMSE of emission image reconstructions (a) frame by frame and (b) total. Notice that images generated using PICD reconstructed parameters have the lowest RMSE.

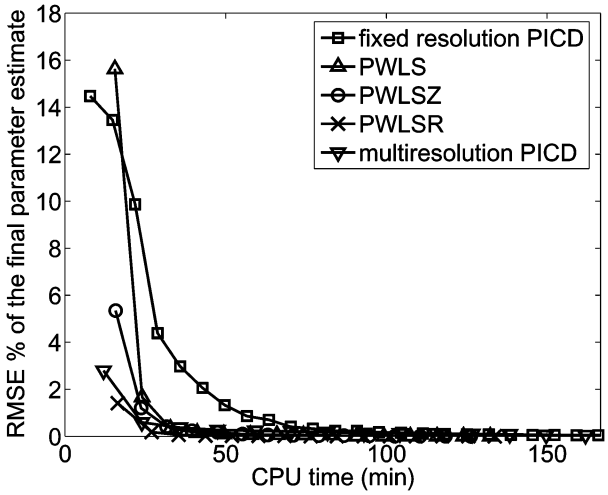

Fig. 12. Convergence curves for the estimation algorithms. Notice that the parametric reconstruction method with multiresolution initialization converges much faster than fixed resolution parametric reconstruction, and it is comparable in speed to the image-domain methods.

PET data for which a kinetic model has been already established. It should be mentioned that there is nothing to prevent us from incorporating more complicated kinetic models into

APPENDIX

PSEUDOCODE

$\varphi \leftarrow$ ParametricReconstruct(sinograms){
 for each iteration {
  for each voxel s {
   $[\theta_1, \theta_2] \leftarrow$ ComputeDerivatives(sinograms, φ_s)
   $\tilde{\varphi}_s \leftarrow \varphi_s$
   $[\tilde{\alpha}, \tilde{\beta}] \leftarrow$ ConvolveWithPlasma($\tilde{c}_s, \tilde{d}_s, [t_0, \ldots, t_{K-1}], \lambda, V_B, C_P$)
   $\tilde{c}_s \leftarrow \arg\min_{\tilde{c}_s}\{$CostFunction$([\tilde{a}_s, \tilde{b}_s, \tilde{c}_s, \tilde{d}_s], \varphi_s, \alpha, \beta, \theta_1, \theta_2, \{\varphi_r : r \in \partial s\}, W)\}$
   $[\tilde{\alpha}, \tilde{\beta}] \leftarrow$ ConvolveWithPlasma($\tilde{c}_s, \tilde{d}_s, [t_0, \ldots, t_{K-1}], \lambda, V_B, C_P$)
   $[\tilde{a}_s, \tilde{b}_s] \leftarrow$ EstimateAandB($\tilde{\varphi}_s, \varphi_s, \tilde{\alpha}, \tilde{\beta}, \alpha, \beta, \theta_1, \theta_2, \{\varphi_r : r \in \partial s\}, W$)
   $l \leftarrow \arg\min_l\{$CostFunction$([\tilde{a}_s, \tilde{b}_s, \tilde{c}_s + l, \tilde{d}_s + l], \varphi_s, \alpha, \beta, \theta_1, \theta_2, \{\varphi_r : r \in \partial s\}, W)\}$
   $\tilde{c}_s \leftarrow \tilde{c}_s + l$; $\tilde{d}_s \leftarrow \tilde{d}_s + l$
   $[\tilde{\alpha}, \tilde{\beta}] \leftarrow$ ConvolveWithPlasma($\tilde{c}_s, \tilde{d}_s, [t_0, \ldots, t_{K-1}], \lambda, V_B, C_P$)
   $[\tilde{a}_s, \tilde{b}_s] \leftarrow$ EstimateAandB($\tilde{\varphi}_s, \varphi_s, \tilde{\alpha}, \tilde{\beta}, \alpha, \beta, \theta_1, \theta_2, \{\varphi_r : r \in \partial s\}, W$)
   $\varphi_s \leftarrow \tilde{\varphi}_s$
  }
 }
}

cost $\leftarrow$ CostFunction($\tilde{\varphi}_s, \varphi, \alpha, \beta, \theta_1, \theta_2, \{\varphi_r : r \in \partial s\}, W$){
 $[\tilde{\alpha}, \tilde{\beta}] \leftarrow$ ConvolveWithPlasma($\tilde{c}_s, \tilde{d}_s, [t_0, \ldots, t_{K-1}], \lambda, V_B, C_P$)
 $[\tilde{a}_s, \tilde{b}_s] \leftarrow$ EstimateAandB($\tilde{\varphi}_s, \varphi_s, \tilde{\alpha}, \tilde{\beta}, \alpha, \beta, \theta_1, \theta_2, \{\varphi_r : r \in \partial s\}, W$)
 cost $\leftarrow$ DeltaCost($\tilde{\varphi}_s, \varphi_s, \tilde{\alpha}, \tilde{\beta}, \alpha, \beta, \theta_1, \theta_2, \{\varphi_r : r \in \partial s\}, W$)
}

$[\tilde{a}, \tilde{b}] \leftarrow$ EstimateAandB($\tilde{\varphi}_s, \varphi_s, \tilde{\alpha}, \tilde{\beta}, \alpha, \beta, \theta_1, \theta_2, \{\varphi_r : r \in \partial s\}, W$){
 for $L_{ab}/3$ iterations {
  $\Delta C \leftarrow$ DeltaCost($[\tilde{a}, \tilde{b}, \tilde{c}_s, \tilde{d}_s], \varphi_s, \tilde{\alpha}, \tilde{\beta}, \alpha, \beta, \theta_1, \theta_2, \{\varphi_r : r \in \partial s\}, W$)
  $(dC/da) \leftarrow (-1/\epsilon)\{$DeltaCost$([\tilde{a} + \epsilon, \tilde{b}, \tilde{c}_s, \tilde{d}_s], \varphi_s, \tilde{\alpha}, \tilde{\beta}, \alpha, \beta, \theta_1, \theta_2, \{\varphi_r : r \in \partial s\}, W) - \Delta C\}$
  $(dC/db) \leftarrow (-1/\epsilon)\{$DeltaCost$([\tilde{a}, \tilde{b} + \epsilon, \tilde{c}_s, \tilde{d}_s], \varphi_s, \tilde{\alpha}, \tilde{\beta}, \alpha, \beta, \theta_1, \theta_2, \{\varphi_r : r \in \partial s\}, W) - \Delta C\}$
  if $\tilde{a} = 0$ and $(dC/da) < 0$ then $(dC/da) \leftarrow 0$
  if $\tilde{b} = 0$ and $(dC/db) < 0$ then $(dC/db) \leftarrow 0$
  if $\{|(dC/da)| + |(dC/db)|\} > 0$ then {
   $((dC/da), (dC/db)) \leftarrow ((dC/da), (dC/db))/\sqrt{((dC/da)^2 + (dC/db))^2}$
   $\zeta \leftarrow \arg\min_{\zeta \in [0,1]}$ DeltaCost$([\tilde{a} + \zeta(dC/da), \tilde{b} + \zeta(dC/db), \tilde{c}_s, \tilde{d}_s], \varphi_s, \tilde{\alpha}, \tilde{\beta}, \alpha, \beta, \theta_1, \theta_2, \{\varphi_r : r \in \partial s\}, W)$
   $\tilde{a} \leftarrow \tilde{a} + \zeta(dC/da); \tilde{b} \leftarrow \tilde{b} + \zeta(dC/db)$
  }
 }
}

$\Delta C \leftarrow$ DeltaCost($\tilde{\varphi}_s, \varphi_s, \tilde{\alpha}, \tilde{\beta}, \alpha, \beta, \theta_1, \theta_2, \{\varphi_r : r \in \partial s\}, W$){
 $\Delta f \leftarrow \tilde{a}_s\tilde{\alpha} + \tilde{b}_s\tilde{\beta} - a_s\alpha - b_s\beta$
 $\Delta C \leftarrow \Delta f\theta_1 + (1/2)\|\Delta f\|^2_{\theta_2} + \sum_{r \in \partial s} g_{s-r}\|T(\tilde{\varphi}_s) - T(\varphi_r)\|^2_W$
}.

---

the PICD algorithm. Even though the solution to these models cannot be expressed in closed form, the power of our method, to decouple the (numerical) solution of the model from the other steps in the optimization procedure, is preserved.

We also believe that an extension of the PICD algorithm to list-mode data is possible. The function $f(\varphi_s)$, defined in (16), can be viewed as the coefficients of a zeroth-order piece-wise constant spline. By using higher order splines, the activity of a voxel at any time can be computed. In this way, event arrival times can be incorporated into the probability function and log likelihood given in (19) and (20) respectively. In this case, $f(\varphi_s)$ would denote the spline coefficients for voxel s, and the quantities θ_1 and θ_2 would be the first and second derivatives of the likelihood function with respect to the spline coefficients.

Our current implementation of direct reconstruction has certain limitations. For example, in image domain estimation methods it is possible to register the images for motion compensation. External measurement devices can allow us to

record motion during acquisition [66] and correct the data in an automated fashion. The current implementation of our algorithm does not allow for this type of compensation. Another limitation is that our method assumes that all voxels are well modeled by the same family of model kinetics, which might not be the case in practice. However we note that single families of model kinetics have been sufficient for describing receptor ligands in different regions of the brain on an ROI-basis.

VIII. Conclusion

In this paper, we introduce a method for the direct reconstruction of kinetic parameters at each voxel from dynamic PET sinogram data. Our algorithm, which we call parametric iterative coordinate decent (PICD), decouples the nonlinearities between the tomographic model, the kinetic model, and the regularized parameters. It also allows one to regularize with respect any desired parametrization, even if the parameters that are selected are nonlinearly related to the projections or the kinetic model parameters. Using an anatomically and physiologically realistic small animal phantom, we demonstrated that our method can reduce the mean squared error in model parameter estimates; and we show that for our example, it does not require substantially more computation than more conventional methods for computing dense parameter estimates in the image domain.

Appendix

See pseudocode at the top of the previous page.

Acknowledgment

The authors would like to thank C. Constantinescu, C. Wang, Dr. K. Yoder, and Dr. T.-Q. Li at Indiana University School of Medicine for their help in constructing the rat phantom from MR data.

References

[1] R. E. Carson and K. Lange, "The EM parametric image reconstruction algorithm," *J. Am. Statist. Assoc.*, vol. 80, no. 389, pp. 20–22, 1985.

[2] M. Kamasak, C. A. Bouman, E. D. Morris, and K. Sauer, "Direct reconstruction of kinetic parameter images from dynamic PET data," in *Proc. 37th Asilomar Conf. Signals, Systems and Computers*, Pacific Grove, CA, Nov. 9–12, 2003, pp. 1919–1923.

[3] B. T. Christian, T. Narayanan, B. Shi, E. D. Morris, J. Mantil, and J. Mukherjee, "Measuring the *in vivo* binding parameters of $[18F]$-Fallypride in monkeys using a PET multiple-injection protocol," *J. Cereb. Blood Flow Metab.*, vol. 24, no. 3, pp. 309–322, 2004.

[4] S. C. Huang and M. E. Phelps, "Principles of tracer kinetic modeling in positron emission tomography," in *Positron Emission Tomography and Autoradiography*, M. E. Phelps, J. Mazziotta, and H. Schelbert, Eds. New York: Raven, 1986, pp. 287–346.

[5] E. D. Morris, C. J. Endres, K. C. Schmidt, B. T. Christian, R. F. M. Jr, and R. E. Fisher, "Kinetic modeling in PET," in *Emission Tomography: The Fundamentals of PET and SPECT*, M. Wernick and J. Aarsvold, Eds. San Diego: Academic, 2004, ch. 23.

[6] R. E. Carson, "Tracer kinetic modeling in PET," in *Positron Emission Tomography, Basic Science and Clinical Practice*, P. E. Valk, D. L. Bailey, D. W. Townsend, and M. N. Maisey, Eds. London, U.K.: Springer, 2002.

[7] S. S. Kety and C. F. Schmidt, "The nitrous oxide method for the quantitative determination of cerebral blood flow in man: Theory, procedure and normal values," *J. Clin. Investagat.*, vol. 27, pp. 476–483, 1948.

[8] L. Sokoloff, M. Reivich, C. Kennedy, M. H. D. Rosiers, C. Patlak, K. D. Pettigrew, O. Sakurada, and M. Shinohara, "The $[14c]$ deoxyglucose method for the measurement of local cerebral glucose utilization: Theory, procedure, and normal values in the conscious and anesthetized albino rat," *J. Neurochem.*, vol. 28, no. 5, pp. 897–916, May 1977.

[9] M. E. Phelps, S. C. Huang, E. J. Hoffman, C. Selin, L. Sokoloff, and D. E. Kuhl, "Tomographic measurement of local cerebral glucose metabolic rate in humans with (f-18)2-fluoro-2-deoxy-d-glucose: Validation of method," *Ann. Neurol.*, vol. 6, no. 5, pp. 371–388, Nov. 1979.

[10] M. A. Mintun, M. E. Raichle, M. R. Kilbourn, G. F. Wooten, and M. J. Welch, "A quantitative model for the *in vivo* assessment of drug binding sites with positron emission tomography," *Ann. Neurol.*, vol. 15, pp. 217–227, 1984.

[11] G. Blomqvist, S. Pauli, L. Farde, L. Ericksson, A. Persson, and C. Halldin, "Dynamic models of reversible ligand binding," in *Clinical Research and Clinical Diagnosis*, C. Beckers, A. Goffiet, and A. Bol, Eds. Norwell, MA: Kluwer, 1989.

[12] V. Cunningham, S. P. Hume, G. R. Price, R. G. Ahier, J. E. Cremer, and A. K. Jones, "Compartmental analysis of diprenorphine binding to opiate receptors in the rat *in vivo* and its comparison with equilibrium data *in vitro*," *J. Cereb. Blood Flow Metab.*, vol. 11, no. 1, pp. 1–9, 1991.

[13] S. P. Hume, R. Myers, P. M. Bloomfield, J. Opacka-Juffry, J. E. Cremer, R. G. Ahier, S. K. Luthra, D. J. Brooks, and A. A. Lammertsma, "Quantitation of carbon-11-labeled raclopride in rat striatum using positron emission tomography," *Synapse*, vol. 27, pp. 4754–4754, 1992.

[14] A. A. Lammertsma, C. J. Bench, S. P. Hume, S. Osman, K. Gunn, D. J. Brooks, and R. S. Frackowiak, "Comparison of methods for analysis of clinical $[11c]$ raclopride studies," *J. Cereb. Blood Flow Metab.*, vol. 16, no. 1, pp. 4252–4252, 1996.

[15] A. A. Lammertsma and S. P. Hume, "Simplfied reference tissue model for PET receptor studies," *NeuroImage*, vol. 4, pp. 153–158, 1996.

[16] R. N. Gunn, A. A. Lammertsma, S. P. Hume, and V. J. Cunningham, "Parametric imaging of ligand-receptor binding in PET using a simplified reference region model," *NeuroImage*, vol. 6, no. 4, pp. 279–287, 1997.

[17] H. Watabe, R. E. Carson, and H. Iida, "The reference tissue model: Three compartments for the reference region," *NeuroImage*, vol. 11, no. 6, pp. S12–S12, 2000.

[18] J. Logan, J. S. Fowler, N. D. Volkow, A. P. Wolf, D. J. S. S. L. Dewey, R. R. MacGregor, R. Hitzemann, S. J. G. B. Bendriem, and D. R. Christman, "Graphical analysis of reversible radioligand binding from time-activity measurements applied to [n-11c-methyl]-(-)-cocaine PET studies in human subjects," *J. Cereb. Blood Flow Metab.*, vol. 10, no. 5, pp. 740–747, 1990.

[19] J. A. Thie, G. T. Smith, and K. F. Hubner, "Linear least squares compartmental-model-independent parameter identification in PET," *IEEE Trans. Med. Imag.*, vol. 16, no. 1, pp. 11–16, Feb. 1997.

[20] K. Chen, M. Lawson, E. Reiman, A. Cooper, D. Feng, S. C. Huang, D. Bandy, and D. Ho, "Generalized linear least squares method for fast generation of myocardial blood flow parametric images with n-13 ammonia PET," *IEEE Trans. Medical Imaging*, vol. 17, no. 2, pp. 236–243, Apr. 1998.

[21] R. E. Carson, S. C. Huang, and M. V. Green, "Weighted integration method for local cerebral blood flow measurements with positron emission tomography," *J. Cereb. Blood Flow Metab.*, vol. 6, pp. 245–258, 1986.

[22] C. S. Patlak and R. G. Blasberg, "Graphical evaluation of blood-to-brain transfer constants from multiple-time uptake data: Generalizations," *J. Cereb. Blood Flow Metab.*, vol. 5, pp. 584–590, 1985.

[23] D. Fang, Z. Wang, and S. C. Huang, "A study on statistically reliable and computationally efficient algorithms for generating local cerebral blood flow parametric images with positron emission tomography," *IEEE Trans. Med. Imag.*, vol. 12, no. 2, pp. 182–188, Jun. 1993.

[24] G. T. Gullberg, "Dynamic SPECT imaging: Exploring a new frontier in medical imaging," in *Proc. IEEE Int. Symp. Biomedical Imaging*, Arlington, VA, Apr. 15–18, 2004, pp. 607–610.

[25] F. O'Sullivan and A. Saha, "Use of ridge regression for improved estimation of kinetic constants from PET data," *IEEE Trans. Med. Imag.*, vol. 18, no. 2, pp. 115–125, Feb. 1999.

[26] S. C. Huang and Y. Zhou, "Spatially-coordinated regression for image-wise model fitting to dynamic PET data for generating parametric images," *IEEE Trans. Nucl. Sci.*, vol. 45, no. 3, pp. 1194–1199, Jun. 1998.

[27] Y. Zhou and S. C. Huang, "Linear ridge regression with spatial constraint for generation of parametric images in dynamic positron emission tomography studies," *IEEE Trans. Nucl. Sci.*, vol. 48, no. 1, pp. 125–130, Feb. 2001.

[28] Y. Zhou, C. Endres, J. Brasic, S. Huang, and D. Wong, "Linear regression with spatial constraint to generate parametric images of ligand-receptor dynamic PET studies with a simplified reference tissue model," *NeuroImage*, vol. 18, pp. 975–989, 2003.

[29] M. S. Y. Kimura and N. Alpert, "Fast formation of statistically reliable FDG parametric images based on clustering and principal components," *Phys. Med. Biol.*, vol. 47, pp. 455–468, Aug. 2002.

[30] Y. Zhou, S. Huang, M. Bergsneider, and D. F. Wong, "Improved parametric image generation using spatial-temporal analysis of dynamic PET studies," *NeuroImage*, vol. 15, pp. 697–707, 2002.

[31] C.-M. Kao, J. T. Yap, J. Mukherjee, and M. Wernick, "Image reconstruction for dynamic PET based on low-order approximation and restoration of the sinogram," *IEEE Trans. Med. Imag.*, vol. 16, no. 6, pp. 738–749, Dec. 1997.

[32] M. V. Narayanan, M. A. King, M. N. Wernick, C. L. Byrne, E. J. Soares, and P. H. Pretorius, "Improved image quality and computation reduction in 4d reconstruction of cardiac-gated SPECT images," *IEEE Trans. Med. Imag.*, vol. 19, no. 5, pp. 423–433, May 2000.

[33] M. N. Wernick, E. J. Infusino, and M. Milosevic, "Fast spatio-temporal image reconstruction for dynamic PET," *IEEE Trans. Med. Imag.*, vol. 18, no. 3, pp. 185–195, Mar. 1999.

[34] T. E. Nichols, J. Qi, E. Asma, and R. M. Leahy, "Spatiotemporal reconstruction of list-mode PET data," *IEEE Trans. Med. Imag.*, vol. 21, no. 4, pp. 396–404, Apr. 2002.

[35] B. W. Reutter, G. T. Gullberg, and R. H. Huesman, "Direct least-squares estimation of spatiotemporal distributions from dynamic SPECT projections using a spatial segmentation and temporal b-splines," *IEEE Trans. Nucl. Sci.*, vol. 19, no. 5, pp. 434–450, May 2000.

[36] ——, "Accuracy and precision of compartmental model parameters obtained from directly estimated dynamic SPECT time-activity curves," *IEEE Trans. Nucl. Sci.*, vol. 51, no. 1, pp. 170–176, Feb. 2004.

[37] L. Shepp and Y. Vardi, "Maximum likelihood reconstruction for emission tomography," *IEEE Trans. Med. Imag.*, vol. MI-1, no. 2, pp. 113–122, Oct. 1982.

[38] M. A. Limber, M. N. Limber, A. Cellar, J. S. Barney, and J. M. Borwein, "Direct reconstruction of functional parameters for dynamic SPECT," *IEEE Trans. Nucl. Sci.*, vol. 42, no. 4, pp. 1249–1256, Aug. 1995.

[39] G. L. Zeng, G. T. Gullberg, and R. H. Huesman, "Using linear time-invariant system theory to estimate kinetic parameters directly from projection measurements," *IEEE Trans. Nucl. Sci.*, vol. 42, no. 6, pp. 2339–2346, Dec. 1995.

[40] A. R. Formiconi, "Least squares algorithm for region-of-interest evaluation in emission tomography," *IEEE Trans. Med. Imag.*, vol. 12, no. 1, pp. 90–100, Mar. 1993.

[41] E. Vanzi, A. R. Formiconi, D. Bindi, G. L. Cava, and A. Pupi, "Kinetic parameter estimation from renal measurements with a three-headed SPECT system: A simulation study," *IEEE Trans. Med. Imag.*, vol. 23, no. 3, pp. 363–373, Mar. 2004.

[42] R. H. Huessman, B. W. Reutter, G. L. Zeng, and G. T. Gullberg, "Kinetic parameter estimation from SPECT cone-beam projection measurements," in *Int. Meeting Fully 3-D Image Reconstruction Conf. Rec.*, 1997, pp. 121–125.

[43] P.-C. Chiao, W. L. Rogers, N. H. Clinthorne, J. A. Fessler, and A. O. Hero, "Model-based estimation for dynamic cardiac studies using ECT," *IEEE Trans. Med. Imag.*, vol. 13, no. 2, pp. 217–226, Jun. 1994.

[44] P.-C. Chiao, W. Rogers, J. Fessler, N. Clinthorne, and A. Hero, "Model-based estimation with boundary side information or boundary regularization," *IEEE Trans. Med. Imag.*, vol. 13, no. 2, pp. 227–234, Jun. 1994.

[45] S. R. Meikle, J. C. Matthews, V. J. Cunningham, D. L. Bailey, L. Livieratos, T. Jones, and P. Price, "Parametric image reconstruction using spectral analysis of PET projection data," *Phys. Med. Biol.*, vol. 43, pp. 651–666, 1998.

[46] J. Matthews, D. Bailey, P. Price, and V. Cunningham, "The direct calculation of parametric images from dynamic PET data using maximum-likelihood iterative reconstruction," *Phys. Med. Biol.*, vol. 42, pp. 1155–1173, 1997.

[47] R. E. Carson, "A maximum likelihood method for region-of-interest evaluation in emission tomography," *J. Comput. Assist. Tomogr.*, vol. 10, no. 4, pp. 654–663, 1986.

[48] T. Farncombe, A. Celler, C. Bever, D. Noll, J. Maeght, and R. Harrop, "The incorporation of organ uptake into dynamic SPECT (dSPECT) image reconstruction," *IEEE Trans. Nucl. Sci.*, vol. 48, no. 1, pp. 3–9, Feb. 2001.

[49] M. Liptrot, K. H. Adams, L. Martiny, L. H. Pinborg, M. N. Lonsdale, N. V. Olsen, S. Holm, C. Svarer, and G. M. Knudsen, "Cluster analysis in kinetic modeling of the brain: A noninvasive alternative to arterial sampling," *NeuroImage*, vol. 21, no. 2, pp. 483–493, 2004.

[50] L. M. Wahl, M. C. Asselin, and C. Nahmias, "Regions of interest in the venous sinuses as input functions for quantitative PET," *J. Nucl. Med.*, vol. 40, no. 10, pp. 1666–1675, 1999.

[51] K. Chen, D. Bandy, E. Reiman, S. C. Huang, M. Lawson, D. Feng, L. Yun, and A. Palant, "Noninvasive quantification of the cerebral metabolic rate for glucose using positron emission tomography, 18F-fluoro-2deoxyglucose, the patlak method, and an image-derived input function," *J. Cereb. Blood Flow Metab.*, vol. 18, no. 7, pp. 716–723, 1998.

[52] D. Feng, K.-P. Wong, C.-M. Wu, and W.-C. Siu, "A technique for extracting physiological parameters and the required input function simultaneously from PET image measurements: Theory and simulation study," *IEEE Trans. Inf. Technol. Biomed.*, vol. 1, pp. 243–254, Dec. 1997.

[53] K.-P. Wong, D. Feng, S. R. Meikle, and M. J. Fulham, "Simultaneous estimation of physiological parameters and the input function—*In vivo* PET data," *IEEE Trans. Inf. Technol. Biomed.*, vol. 5, pp. 67–76, Mar. 2001.

[54] C. A. Bouman and K. Sauer, "A unified approach to statistical tomography using coordinate descent optimization," *IEEE Trans. Image Processing*, vol. 5, no. 3, pp. 480–492, Mar. 1996.

[55] E. Mumcuoglu, R. M. Leahy, S. Cherry, and E. Hoffman, "Accurate geometric and physical response modeling for statistical image reconstruction in high resolution PET scanners," in *Proc. IEEE Nuclear Science Symp./Medical Imaging Conf.*, 1996, pp. 1569–1573.

[56] T. Frese, N. C. Rouze, C. A. Bouman, K. Sauer, and G. D. Hutchins, "Quantitative comparison of FBP, EM, and Bayesian reconstruction algorithms, including the impact of accurate system modeling, for the indyPET scanner," *IEEE Trans. Med. Imag.*, vol. 22, no. 2, pp. 258–276, Feb. 2003.

[57] H. W. Kuhn and A. W. Tucker, "Nonlinear programming," in *Proc. 2nd Berkeley Symp. Mathematical Statistics and Probabilistics*, 1951, pp. 481–492.

[58] K. Sauer and C. A. Bouman, "A local update strategy for iterative reconstruction from projections," *IEEE Trans. Signal Processing*, vol. 41, no. 2, pp. 534–548, Feb. 1993.

[59] G. Paxinos and C. Watson, *The Rat Brain in Stereotaxic Coordinates*, 4th ed. New York: Academic, 1998.

[60] S. Pappata, S. Dehaene, J. B. Poline, M. C. Gregoire, A. Jobert, J. Delforge, V. Frouin, M. Bottlaender, F. Dolle, L. D. Giamberardino, and A. Syrota, "*In vivo* detection of striatal dopamine release during reward: A PET study with $[^{11}C]$ raclopride and a single dynamic scan approach," *NeuroImage*, vol. 16, no. 4, pp. 1015–1027, 2002.

[61] S. S. Saquib, C. A. Bouman, and K. Sauer, "ML parameter estimation for Markov random fields with applications to Bayesian tomography," *IEEE Trans. Image Processing*, vol. 7, no. 7, pp. 1029–1044, Jul. 1998.

[62] H. Hudson and R. Larkin, "Accelerated image reconstruction using ordered subsets of projection data," *IEEE Trans. Med. Imag.*, vol. 13, no. 4, pp. 601–609, Dec. 1994.

[63] M. Slifstein and M. Laruelle, "Effects of statistical noise on graphical analysis of PET neuroreceptor studies," *J. Nucl. Med.*, vol. 41, no. 12, pp. 2083–2088, 2000.

[64] M. Ichise, H. Toyama, R. B. Innis, and R. E. Carson, "Strategies to improve neuroreceptor parameter estimation by linear regression analysis," *J. Cereb. Blood Flow Metab.*, vol. 22, pp. 1271–1281, 2002.

[65] J. Logan, J. S. Fowler, N. D. Volkow, Y. S. Ding, G. J. Wang, and D. L. Alexoff, "A strategy for removing the bias in the graphical analysis method," *J. Cereb. Blood Flow Metab.*, vol. 21, no. 3, pp. 307–320, 2001.

[66] P. M. Bloomfield, T. J. Spinks, J. Reed, L. Schnorr, A. M. Westrip, L. Livieratos, R. Fulton, and T. Jones, "The design and implementation of a motion correction scheme for neurological PET," *Phys. Med. Biol.*, vol. 48, no. 8, pp. 959–978, 2003.